

Effect of CMC degree of substitution and gliadin/CMC ratio on surface rheology and foaming behavior of gliadin/CMC nanoparticles

Dengfeng Peng^{a,b}, Weiping Jin^d, Miriam Arts^a, Jack Yang^a, Bin Li^{b,c}, Leonard M.C. Sagis^{a,*}

^a Laboratory of Physics and Physical Chemistry of Foods, Wageningen University, Bornse Weiland 9, 6708WG, Wageningen, the Netherlands

^b College of Food Science and Technology, Huazhong Agricultural University, Wuhan, Hubei, 430070, PR China

^c Key Laboratory of Environment Correlative Dietology (Huazhong Agricultural University), Ministry of Education, Wuhan, Hubei, 430070, PR China

^d College of Food Science and Engineering, Wuhan Polytechnic University, Wuhan, Hubei, 430023, PR China

ARTICLE INFO

Keywords:

Foam
Surface behavior
Nanoparticle
Structure
Degree of substitution
Ratio

ABSTRACT

To understand the influence of the degree of substitution (DS) of sodium carboxymethyl cellulose (CMC) and gliadin:CMC ratio on the surface and foaming behaviors of gliadin-CMC nanoparticles (G-CMC NPs) at pH 3, three DS (0.7–1.2) and four ratios (G:CMC~1:0.5–1:2) were investigated. Gliadin NPs with a pH of 3 were utilized as a control. Results showed that G-CMC NPs at all investigated DS and ratios possessed higher foamability and foam stability when compared to the control. This indicated that adding CMC to gliadin NP suspensions could greatly improve their foaming properties. G-CMC NPs with a DS of 0.7 and 0.9, had lower surface charge than G-CMC1.2 NPs, resulting in a weaker electrostatic repulsion, thus leading to faster adsorption kinetics and higher foamability. By increasing the G:CMC ratio from 1:0.5 to 1:2, the particle size gradually rose, and the zeta potential remained unchanged. At a ratio of 1:2, the highest foam stability was observed. This might be ascribed to the high continuous phase viscosity at this ratio, which could slow down the drainage rate and protect the bubbles against coalescence and disproportionation. It was worth mentioning that G-CMC NPs at all ratios exhibited impressive foamability (~220%) even at a very low concentration of G-CMC NPs (gliadin was fixed at 1 mg/mL). This implies that G-CMC NPs could act as a new efficient foaming agent, and based on its simple preparation, have the potential to be widely applied in foamed food.

1. Introduction

Liquid foams are interface-dominated systems and have received extensive attention in colloid science, resulting from their wide applications in food products, biological engineering, pharmaceutical formulations, and cosmetic industries (Cristofolini, Orsi, & Isa, 2018; Wege, Kim, Paunov, Zhong, & Velez, 2008; Wu et al., 2018). Foams belong to the class of thermodynamically unstable systems, so foaming agents which act as surface-active components are required to form and stabilize foams (Brush & Roper, 2008; Dollet & Raufaste, 2014; Salonen, In, Emile, & Saint-Jalmes, 2010). In food, surfactants and proteins are the most commonly used foaming agents. Many of these two types of foaming agents have some drawbacks. For example, most surfactants have relatively poor foam stability. Commonly used proteins, such as milk and egg proteins, cannot be applied in vegetarian foods. Some plant proteins, such as soy and pea proteins, require relatively high concentrations to stabilize foams. Hence, studies of new effective foaming

agents which can be applied in vegan or more sustainably produced foods are of scientific significance. Recently, nanoparticles (NPs) prepared by the assembly of natural polymers with appropriate surface activities have been suggested as attractive alternatives, due to their unique surface behaviors and high foam stability (Ellis, Norton, Mills, & Norton, 2017; Asghari, Norton, Mills, Sadd, & Spyropoulos, 2016; Schmitt, Bovay, & Rouvet, 2014; Jin et al., 2012). They can adsorb quickly to the air/water interface, and develop viscoelastic adsorbed layers to stabilize foams.

Proteins are often selected as candidates to form particles, resulting from their amphiphilicity and biodegradability. Water-soluble proteins are the most frequently utilized materials, such as soy protein isolate with good water solubility (Matsumiya & Murray, 2016; Morales, Martínez, Ruiz-Henestrosa, & Pilosof, 2015) and whey protein (Schmitt, Bovay, Rouvet, Shojaei-Rami, & Kolodziejczyk, 2007; Schmitt et al., 2014; Jambrak, Mason, Lelas, Paniwnyk, & Herceg, 2014). However, these also face inevitable limitations, owing to the high water solubility

* Corresponding author.

E-mail address: leonard.sagis@wur.nl (L.M.C. Sagis).

<https://doi.org/10.1016/j.foodhyd.2020.105955>

Received 20 November 2019; Received in revised form 15 April 2020; Accepted 15 April 2020

Available online 21 April 2020

0268-005X/© 2020 The Authors. Published by Elsevier Ltd. This is an open access article under the CC BY license (<http://creativecommons.org/licenses/by/4.0/>).

and insufficient surface activity of the resulting particles, which cause them to have relatively poor foaming properties. Gliadin, an alcohol-soluble protein obtained from wheat, is suitable for producing particles and overcomes the disadvantages mentioned above, resulting from its water insolubility and high surface activity (Banc et al., 2007; Zhou et al., 2019). Colloidal particles prepared from gliadin have promising foaming behavior, significantly better than that of ovalbumin and sodium caseinate, which are widely used in food (Peng et al., 2017). It is a readily available plant-derived protein, and is easy to fabricate through green and simple methods. Therefore, it has potential application value in foamed food products. Many foods have acidic pH values, less than 7 at 25 °C. Gliadin particles are sensitive to pH, and do not stabilize foams well at low acidic pH values, such as pH 3 (Peng et al., 2018). In order to broaden their application in food, it is significant to improve the foaming properties of gliadin particles at acidic pH. It has been suggested that using polysaccharides in combination with gliadin to form polymeric complex nanoparticles could improve functionality at acidic conditions. A potential candidate polysaccharide is sodium carboxymethyl cellulose (CMC), a cellulose derivative obtained by etherification of the hydroxyl groups in cellulose with methylcarboxyl groups, due to its wide availability and attractive functional properties (Gibis, Schuh, & Weiss, 2015). Some researchers have used CMC to form particles with alcohol-soluble proteins such as zein, to improve their functional properties (Liang et al., 2015; Babazadeh, Tabibiazar, Hamishehkar, & Shi, 2019). The charge distribution of CMC, which has a negative charge, is closely related to its degree of substitution (DS, defined as carboxymethyl groups per repeating unit) (Jia et al., 2014). The DS of CMC, therefore, has a strong influence on the structure and function of complexes formed by protein and CMC (Xiong, Deng, Li, Li, & Zhong, 2020; Li et al., 2017). For complex particles formed by self-assembly of gliadin and CMC, the relation between DS of CMC and gliadin:CMC ratio and foaming behavior has so far not been investigated.

In this work, a systematic study is presented in which the effects of DS of CMC and ratio (G:CMC) on the particle physical properties (particle size, zeta potential, and viscosity), on surface properties of air-water interfaces stabilized by G-CMC NPs (surface pressure, surface dilatational behavior, and viscoelastic response at large amplitude), and foaming properties (foamability, foam stability, liquid volume in the foam, and microstructure of bubble) of G-CMC NPs were investigated. In addition, the relationship among these three properties was investigated to further understand the formation and stabilization mechanisms of foams stabilized by G-CMC NPs.

2. Materials and methods

2.1. Materials

Gliadin with a purity of 90.6% was extracted from gluten as described in previous work (Peng et al., 2017). Sodium carboxymethyl cellulose (CMC) with three DS (0.7, 0.9, and 1.2, average M_w of these three CMC~250,000) was purchased from Sigma-Aldrich Trading Co., Ltd. (Zwijndrecht, Netherlands). All other chemicals, such as ethanol (~100%), hydrochloric acid, and sodium hydroxide, were of analytical grade. Ultrapure water purified by a Milli-Q system (MilliQ Purelab Ultra, Germany) was utilized for all the experiments.

2.2. Preparation of gliadin-CMC nanoparticles

Gliadin with a concentration of 2.5% (w/v) was obtained by dissolving powders in ethanol solution (70%, v/v) in water, at room temperature (~20 °C). CMC powders with three DS (0.7, 0.9, and 1.2) were separately dissolved in ultrapure water to a final stock solution (1%, w/v). For the study of the effects of DS, the ratio of G:CMC was set to 1:1, and the concentration of gliadin in the final solution was 1 mg/mL. To prepare these samples, CMC stock solutions with three DS (0.7, 0.9, and

1.2) were first mixed with weighed ultrapure water. Subsequently, the gliadin solution was rapidly added into CMC solutions from above. The mixed solutions were stirred vigorously for 3 min, and then the pH was adjusted to 3 using HCl (0.5 M, 1 M, and 2 M). For investigating the effect of G:CMC ratio, gliadin and CMC (DS~0.9) mixtures with four weight ratios (1:0.5, 1:0.8, 1:1, and 1:2) were prepared using the same method described above. All these mixed solutions were standardized on 1 mg/mL gliadin. A sample containing only gliadin NPs (1 mg/mL, pH 3) was used as a control.

2.3. Particle size and ζ potential measurements

The particle size distributions and ζ potential of samples were measured using a Zetasizer Ultra (Malvern Instrument Ltd., U.K.) at 20 °C. All samples were carefully loaded in the cuvette to prevent the formation of air bubbles.

2.4. Viscosity measurements

The viscosity of sample solutions was measured with an Ubbelohde Capillary Viscometer (TV 12, PMT, Netherlands). The samples were added into the Ubbelohde and then the Ubbelohde was placed into a precision water bath at 20 °C. After equilibration for 10 min, the time (t) was recorded in which a fixed volume of sample flowed through the capillary. From this the kinematic viscosity (ν) was calculated using equation (1):

$$\nu = Ct \quad (1)$$

where C is a constant equal to $0.009719 \text{ mm}^2 \text{ s}^{-2}$. The viscosity (η) was calculated using equation (2):

$$\eta = \rho\nu \quad (2)$$

where ρ is the density of the sample measured by a density meter (DMA 5000, AntonPaar, Graz, Austria) at 20 °C.

2.5. Surface pressure and surface dilatational rheology

A Profile Analysis Tensiometer (Sinterface Technologies, Germany) was used to measure the surface pressure and surface dilatational modulus of samples at the air/water interface. An axisymmetric drop was formed through a syringe system and controlled by a video camera. The dynamic surface tension was monitored for 3 h, while the area of the drop was kept at 20 mm^2 . The values of the surface tension (γ) were calculated by analyzing the shape of the pendent drop according to the Gauss-Laplace equation. The surface pressure (π) was obtained according to equation (3):

$$\pi = \gamma_s - \gamma_p \quad (3)$$

where γ_s is the surface tension of the pure solvent, and γ_p is the time/dependent surface tension of the samples. All experiments were performed at 20 °C.

The surface dilatational modulus of samples at the air/water interface was determined using the following three oscillation modes:

- (1) Time sweeps, in which the surface elastic modulus (E_d) was recorded as a function of time (t), at an amplitude of 10%, and frequency of 0.05 Hz, for 3 h. The drop was alternately subjected to 5 sinusoidal oscillation cycles, and 5 static cycles.
- (2) Frequency sweeps, in which after an adsorption phase of 3 h, the surface elastic modulus (E_d) was measured at frequencies of 0.01, 0.02, 0.05, and 0.1 Hz, at a constant amplitude of 10%.
- (3) Amplitude sweeps, in which the amplitude was varied from 5, 10, 15, 20, 25, to 30%, at a constant frequency of 0.05 Hz (again after an adsorption phase of 3 h).

2.6. Lissajous plots

The data of the dilatational amplitude sweeps was analyzed using Lissajous plots, according to the method of Sagis et al. (Sagis & Fischer, 2014) and Van Kempen et al. (van Kempen, Schols, van der Linden, & Sagis, 2013). Lissajous plots were prepared by plotting the time dependent surface pressure (π) versus deformation ($\delta A/A_0$), where δA was calculated as:

$$\delta A = A - A_0 \quad (4)$$

where A and A_0 are the area of the deformed and nondeformed interface, respectively.

2.7. Foaming properties

The foamability and foam stability of nanoparticles were determined by the method of Peng et al. (Peng, Yang, Li, Tang, & Li, 2017) with slight modification. Briefly, foams were generated by stirring 15 mL samples placed in a plastic beaker (internal diameter of 33 mm, height of

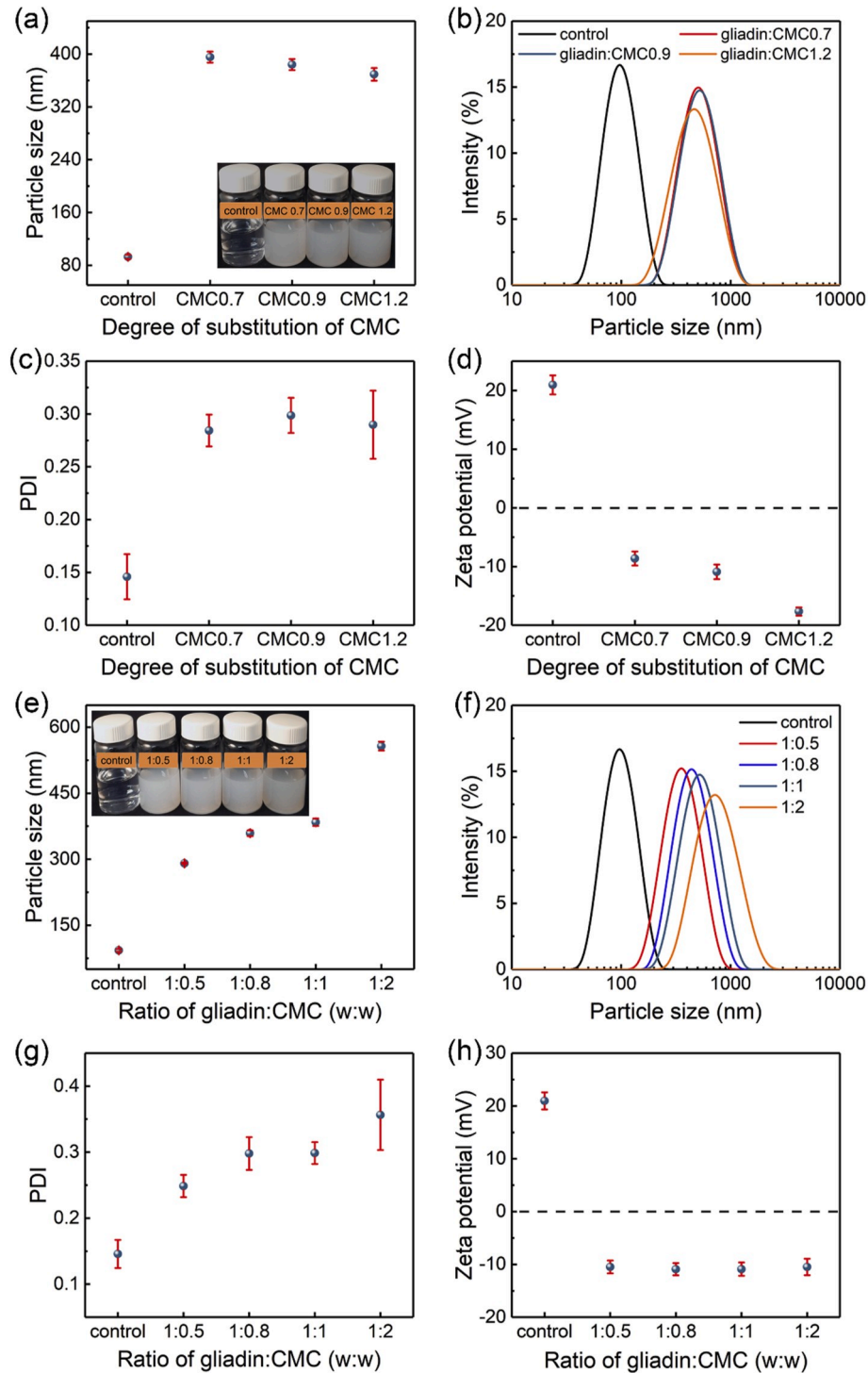


Fig. 1. Particle size (a, e), particle size distribution (b, f), polydispersity index (c, g), and zeta potential (d, h) of the control and G-CMC NPs with different DS of CMC (0.7–1.2) and G:CMC ratio (1:0.5–1:2). The inset images in (a, e) are visual appearance of the control and G-CMC NPs.

80 mm) with an aerolatte head attached to an electric rotator (RW 20 digital, IKA, Germany) at 1500 rpm for 90 s at 20 °C. Subsequently, the foams were immediately transferred to a measuring cylinder (50 mL). Foam and liquid volumes were recorded as a function of time. Foamability (FA) was characterized by comparing the foam volume at 2min (V_2) with the initial liquid volume of samples (15 mL):

$$FA (\%) = \frac{V_2}{15} \times 100 \quad (5)$$

Foam stability (FS) was measured by recording the half-life time ($t_{1/2}$), which was the time for the foam volume to reduce to half of its initial foam volume. The drainage speed of liquid from the foam was determined by recording the volume of the liquid column as a function of time.

2.8. Foam microstructure observation by optical microscopy

The microstructure images of foams after being stored at 20 °C from 30 s to 30 min were visualized using an optical microscope (Axioskop, Germany). The bubbles were obtained from a height of ~3 cm from the bottom of the plastic beaker (internal diameter of 33 mm, height of 80 mm).

2.9. Statistical analysis

All experiments were performed in at least triplicate and the results were recorded as means \pm standard deviations. One-way analysis of variance (ANOVA) was carried out using SPSS 23.0 for estimating the significance of differences among mean values ($p < 0.05$).

3. Results and discussion

3.1. Solution properties of gliadin-CMC nanoparticles

3.1.1. Effect of degree of substitution of CMC

Particle size, zeta potential, and viscosity of the particle suspensions are key parameters to generate large amounts of foams with high stability (Morales et al., 2015; Chen et al., 2016; Murray & Ettelaie, 2004). The effect of the DS of CMC on the solution properties for G-CMC NPs are presented in Fig. 1 a-d and Fig. 2a. Compared with the control, the G-CMC NPs had a larger particle size and a more turbid visual appearance (Fig. 1a). This indicated that gliadin and CMC with different DS formed complex nanoparticles through electrostatic interaction, owing to their opposite charge. The particle size distribution demonstrated that G-CMC NPs with different DS all possessed a nearly monomodal distribution (Fig. 1b). As the DS of CMC increased from 0.7 to 1.2, the particle size of G-CMC NPs displayed a slight decrease from 395 nm to 369 nm,

with similar polydispersity index (PDI) (Fig. 1b and c). After storing solutions at room temperature (20 °C) for 15 days, the particle size of G-CMC NPs with DS of 0.7–1.2 all increased by less than 30 nm, implying that G-CMC NPs were stable (Table S1). The G-CMC NPs with DS of 1.2 had a more pronounced negative charge than the other two nanoparticles ($p < 0.05$) (Fig. 1d). This could be attributed to the higher charge density of CMC with high DS, which after formation of a nanoparticle with gliadin, would result in more charge on the surface of the complex nanoparticle. The G-CMC NP dispersions with different DS had similar viscosity, which was higher than that of the control by a factor of approximately 1.5 (Fig. 2a).

3.1.2. Effect of gliadin-CMC ratio

Fig. 1 e-h presents the particle size, visual appearance, size distribution, PDI, and zeta potential of G-CMC NPs with different ratios (G: CMC~1:0.5–1:2), all standardized on a concentration of gliadin in the final solution of 1 mg/mL. The G-CMC NPs at all ratios presented uniform size distribution. The particle size and PDI significantly increased as the ratio increased from 1:0.5 to 1:2 ($p < 0.05$) (Fig. 1 e-g). After storing for 15 days at room temperature (20 °C), the particle size of G-CMC NPs at all ratios increased by less than 50 nm, implying that they had good stability (Table S2). For all ratios, G-CMC NPs possessed similar negative charge ($p > 0.05$) (Fig. 1h). Increasing the ratio from 1:0.5 to 1:2, the viscosity of the dispersion of complex NPs gradually increased, with a particularly strong increase in going from a ratio of 1:1 to a ratio of 1:2 (Fig. 2b).

3.2. Surface behavior of gliadin-CMC nanoparticles

3.2.1. Effect of degree of substitution of CMC

The dynamic surface pressure (π) is a key factor in determining foamability (Patino, Sanchez, & Niño, 2008). The surface pressure of G-CMC NPs as a function of time is presented in Fig. 3a. Up to 900 s, the values of π for all samples increased quickly, reflecting the rapid adsorption of nanoparticles at the air/water interface. G-CMC NPs with different DS displayed different adsorption kinetics. The adsorption of the particles is governed by several processes, including diffusion towards the interface, penetration into the interface, followed by rearrangements within the interface. Plotting surface pressure as a function of the square root of time (Fig. 3b), we see a straight line in the first few seconds of the adsorption process, indicating that the initial adsorption is diffusion controlled. The slope of the curve (K_{diff}) was used to estimate the adsorption rate in that phase (Liu & Tang, 2014; Wu et al., 2014; Wang et al., 2012). The larger the values of K_{diff} , the faster the adsorption rate of the nanoparticles. As shown in Table 1, K_{diff} of G-CMC NPs with a DS of 0.7 and 0.9 had higher values than that of NPs with a DS of 1.2. This indicated that G-CMC0.7 and G-CMC0.9 NPs possessed a faster

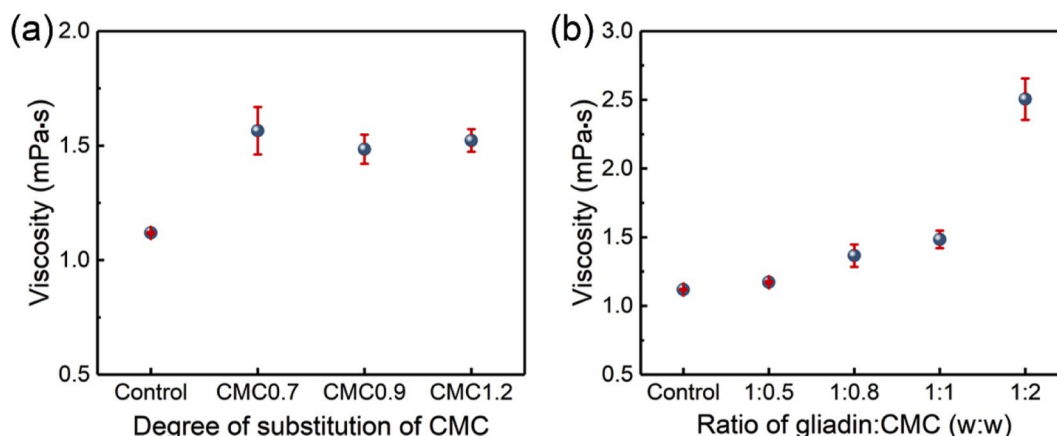


Fig. 2. Viscosities of the control and G-CMC NPs with different DS of CMC (a) and G:CMC ratio (b).

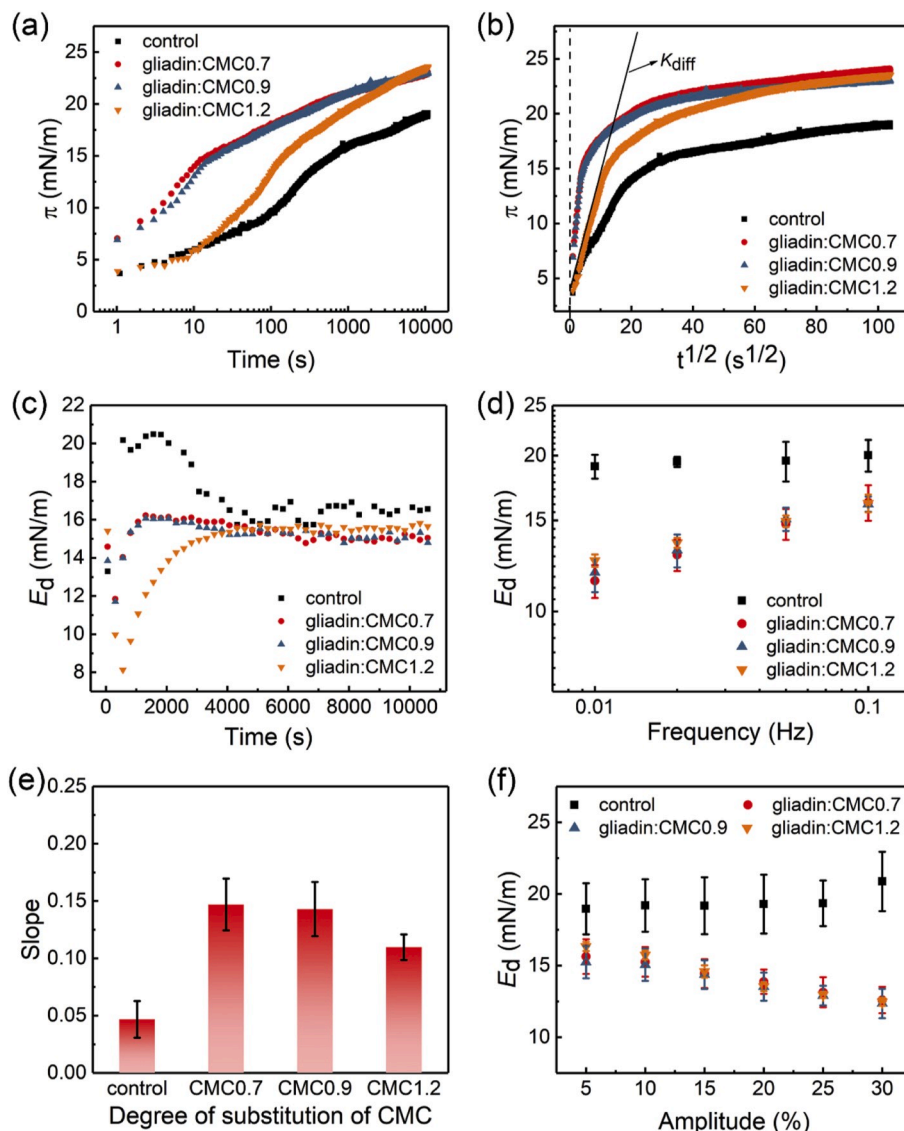


Fig. 3. (a–b) Surface pressure (π) as a function of time for the control and G-CMC NPs with different DS of CMC at the air/water interface (K_{diff} quantifies the diffusion rate). (c) Time evolution of the elastic modulus (E_d) for the adsorption of the control and G-CMC NPs at the air/water interface. (d) E_d as a function of frequency (0.01–0.1 Hz). (e) N-value in $E_d \sim \omega^n$. (f) E_d as a function of amplitude (5–30%).

adsorption rate. In the subsequent phases of adsorption, the surface pressure of the particles with a DS of 0.7 and 0.9 appeared to reach a (nearly) constant value for $t > 1000$ s. The particles with a DS of 1.2 take a much longer time to reach a similar value.

The adsorption rate of particles from the bulk to the air/water interface is related to their microstructural properties, such as zeta potential and particle size (Mahmoudi, Axelos, & Riaublanc, 2011; Peng et al., 2018). In our work, the G-CMC NPs with DS of 0.7–1.2 had a similar particle size. But G-CMC1.2 NPs possessed a higher zeta potential when compared with G-CMC0.7 and G-CMC0.9 NPs. The higher surface charge of these particles, resulting in a stronger electrostatic repulsion between the particles, and between the particles and the interface, is the most likely cause for the slower adsorption rate.

Fig. 3c shows the evolution of the dilatational elastic modulus (E_d) for G-CMC NP stabilized air/water interfaces as a function of time. For the first 2000 s, E_d of all investigated samples increased with time. This reflected that nanoparticles adsorbed at the air/water interface and developed a surface layer with a predominantly elastic response (E_d was significantly larger than the dilatational viscous modulus (data not shown)). At longer times, the E_d of the interface stabilized by the control decreased significantly, implying that the microstructure of the adsorbed layer might be affected by the applied oscillation. The E_d of G-CMC0.7 and G-CMC0.9 displayed only a minor decrease and E_d of G-CMC1.2 was still increasing in this phase of the experiment. This indicated that interfaces stabilized by G-CMC NPs had a less brittle microstructure and hence a larger maximum linear strain than interfaces

Table 1

The diffusion rate (K_{diff}) and linear regression coefficient (LR) for slope of π vs $t_{1/2}$ of adsorption of the control and G-CMC NPs with different DS of CMC (0.7–1.2) and G:CMC ratio (1:0.5–1:2) at the air/water interface.

	control	G-CMC 0.7	G-CMC 0.9	G-CMC 1.2	1:0.5	1:0.8	1:1	1:2
K_{diff}	0.53 ± 0.03	2.32 ± 0.17	2.12 ± 0.12	1.17 ± 0.15	2.22 ± 0.02	2.36 ± 0.11	2.12 ± 0.12	2.19 ± 0.15
LR	0.986 ± 0.004	0.920 ± 0.014	0.977 ± 0.027	0.993 ± 0.001	0.948 ± 0.017	0.959 ± 0.036	0.977 ± 0.027	0.973 ± 0.011

stabilized by gliadin NPs. After 3 h of oscillation, G-CMC NPs with DS of 0.7–1.2 all had comparable E_d .

To examine further the surface rheological properties and surface structure of the adsorption layer, frequency and amplitude sweeps were performed and the corresponding curves are displayed in Fig. 3d and f. For G-CMC NPs with a DS of 0.7–1.2, E_d increased progressively with increasing the frequency from 0.01 to 0.1 Hz, illustrating a frequency-dependent behavior, resulting from relaxation phenomena at the interface (Jin et al., 2017). The curves were analyzed using the scaling relation $E_d \sim \omega^n$, where ω denotes the frequency, and the value of n was determined from the slope of a double logarithmic plot of E_d versus frequency (van Kempen, Schols, van der Linden, & Sagis, 2013). A value of $n = 0$ suggests a completely elastic interface with rubber-like behavior, and a slope of 0.5 implies that the dilatational elasticity is

completely controlled by the diffusion process of the surface active components between bulk and interface, as explained by the Lucassen van den Tempel model (Lucassen & Van Den Tempel, 1972). As can be seen from Fig. 3e, the value of n of the control was close to 0, indicating the surface layer formed by the control displayed an approximate elastic response. The G-CMC NPs with three DS all exhibited higher n values than the control. This illustrated that the surface structure of interfaces stabilized by G-CMC NPs showed a less elastic solid-like response than that of the control. In the amplitude sweeps (Fig. 3f), as the amplitude rose from 5% to 30%, the E_d of G-CMC NP stabilized interfaces with a DS of 0.7–1.2 displayed a gradual small decrease, whereas the modulus of interfaces stabilized by the control was nearly constant. This behavior implied that for the former, the structure of the adsorbed layer was affected by the deformation. The moduli in Fig. 3f are based on the

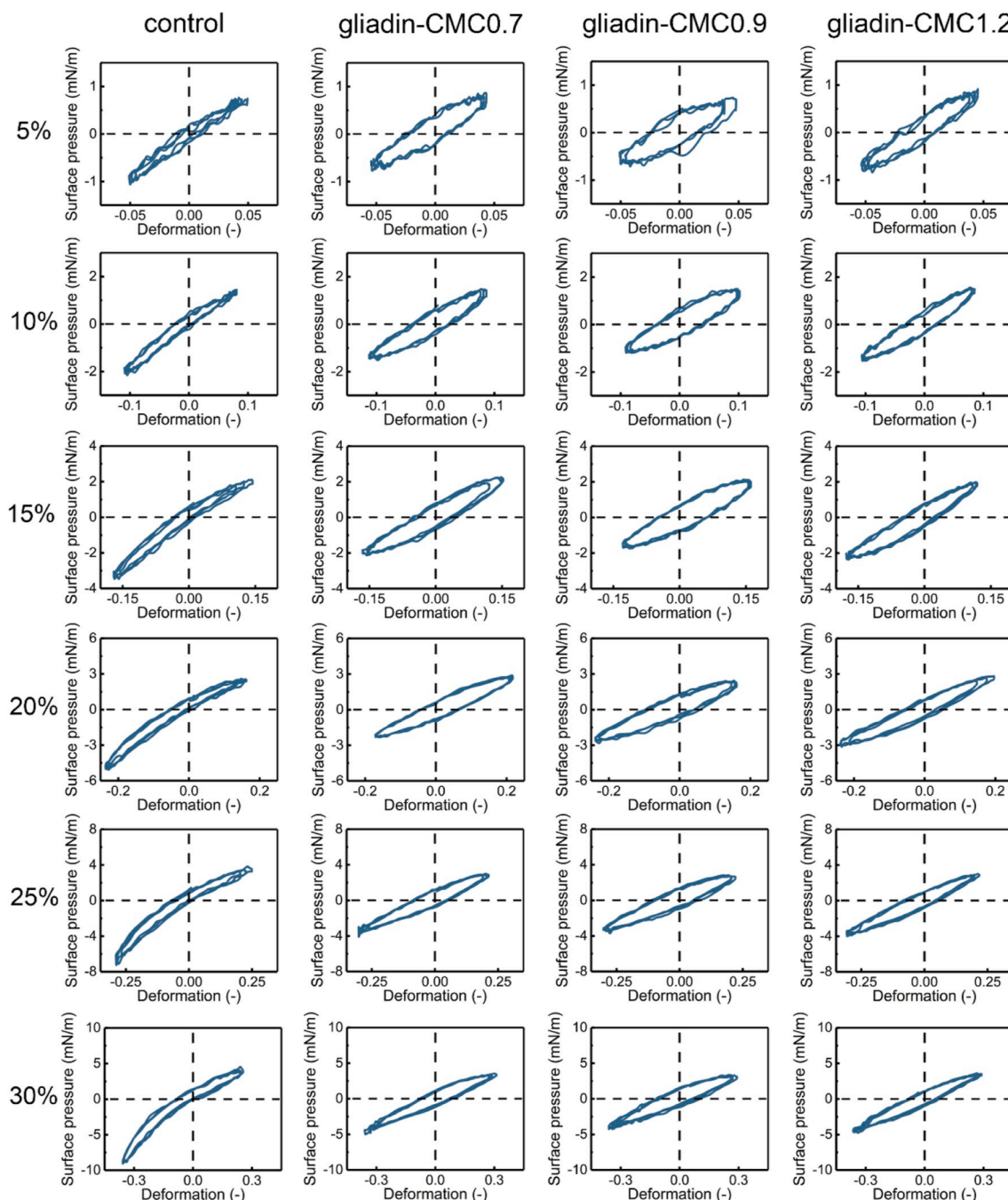


Fig. 4. Lissajous plots obtained during amplitude sweeps (5–30%) of air/water interface formed by the control and G-CMC NPs with different DS of CMC.

intensity and phase of the first harmonic of the Fourier transform of the time dependent surface pressure signal, and the obtained values may, therefore, be inaccurate in the nonlinear regime. We, therefore, constructed Lissajous plots of surface pressure vs deformation, which have been confirmed to be a good analytical tool for investigating the surface behavior in large-amplitude oscillatory deformations (van den Berg, Kuster, Windhab, Sagis, & Fischer, 2018; R  hs, Scheuble, Windhab, & Fischer, 2013; Sagis & Fischer, 2014; Sagis & Scholten, 2014). The plots are presented in Fig. 4. For amplitudes up to 10%, the Lissajous plots for interfaces stabilized by the control were approximately axisymmetric, which points to a linear viscoelastic response. As the amplitude was increased from 15 to 30%, the shape of plots became increasingly asymmetric, implying nonlinear behavior, in which both even and odd harmonics are present in the response. The surface layer showed a strain

softening in extension (upper part of the Lissajous plot), evident from the significant decrease in the tangential modulus (the slope at each point of the cycle), and strain hardening in compression (lower part of the Lissajous plot), this in spite of the linear response obtained from the standard first harmonic based analysis. For interfaces stabilized by G-CMC NPs with a DS of 0.7–1.2, the shape of the Lissajous plots was similar at the same amplitude (5–30%), indicating the DS did not affect the surface behaviors of complex nanoparticles at large deformation. The Lissajous plots for G-CMC NPs were obviously different from those of the control, suggesting that the addition of CMC could change the surface viscoelastic response of gliadin NPs. For amplitudes from 5 to 30%, the maximum values of surface pressure in extension for G-CMC NPs were slightly lower than those in compression, and the Lissajous plots displayed only minor asymmetries. This reflected that the complex

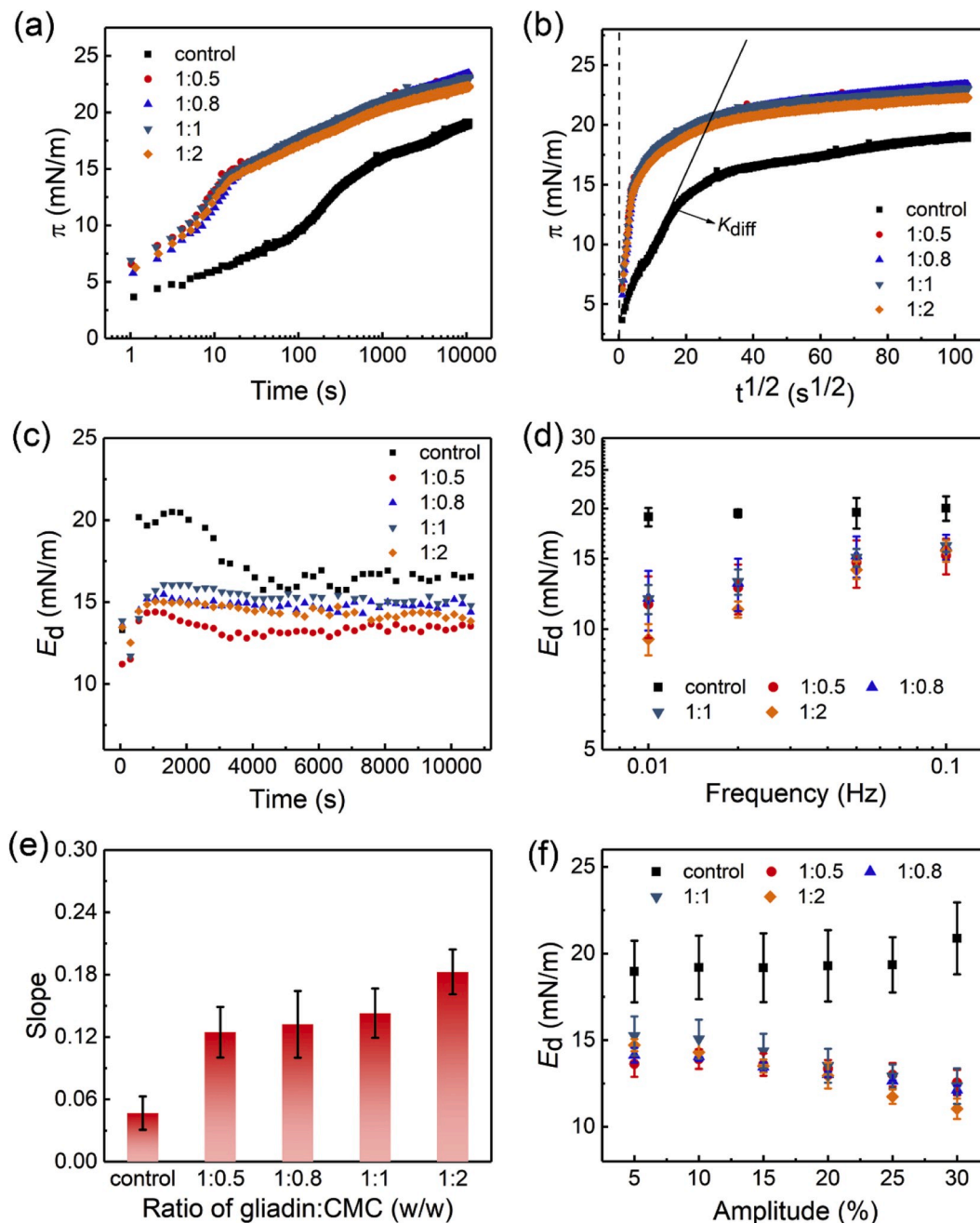


Fig. 5. (a–b) Surface pressure (π) as a function of time for the control and G-CMC NPs with different ratios at the air/water interface (K_{diff} represents the diffusion rate). (c) Time evolution of the elastic modulus (E_d) for the adsorption of the control and G-CMC NPs at the air/water interface. (d) E_d as a function of frequency (0.01–0.1 Hz). (e) N-value in $E_d \sim \omega^n$. (f) E_d as a function of amplitude (5–30%).

nanoparticles still showed a near linear response even at an amplitude of 30%, in accordance with the results from the first harmonic analysis. This behavior was significantly different from the surface behaviors of other proteins or particles, which display more significant nonlinearity in their dilatational response, such as β -lactoglobulin fibrils (Rühs, Affolter, Windhab, & Fischer, 2013) and soy protein fibrils (Wan, Yang, & Sagis, 2016a). The control-stabilized interfaces had a higher dilatational modulus, a near zero value for n in the frequency sweeps, and displayed softening behavior upon extension. This indicated that the interfaces stabilized by gliadin NPs had a denser and more cohesive structure. For the interfaces with G-CMC NPs, the particles apparently form a more mobile and stretchable structure.

3.2.2. Effect of gliadin-CMC ratio on surface behavior

The time evolution of π for G-CMC NPs with different ratios is shown in Fig. 5a. At all ratios, the adsorption behaviors within 3 h were similar, reflecting they had comparable adsorption kinetics, with K_{diff} values all close to ~ 2.2 (Fig. 5b and Table 1). As the ratios increased, the particle size of G-CMC NPs increased significantly, but all ratios had comparable zeta-potential (Fig. 1e and h). This again indicated that the charge of the particles was more important for the adsorption behavior than their size. This phenomenon was consistent with our previous work (Peng et al., 2018).

The time evolution of E_d for G-CMC NPs with different ratios was monitored and shown in Fig. 5c. After 2000 s, the decrease in E_d values

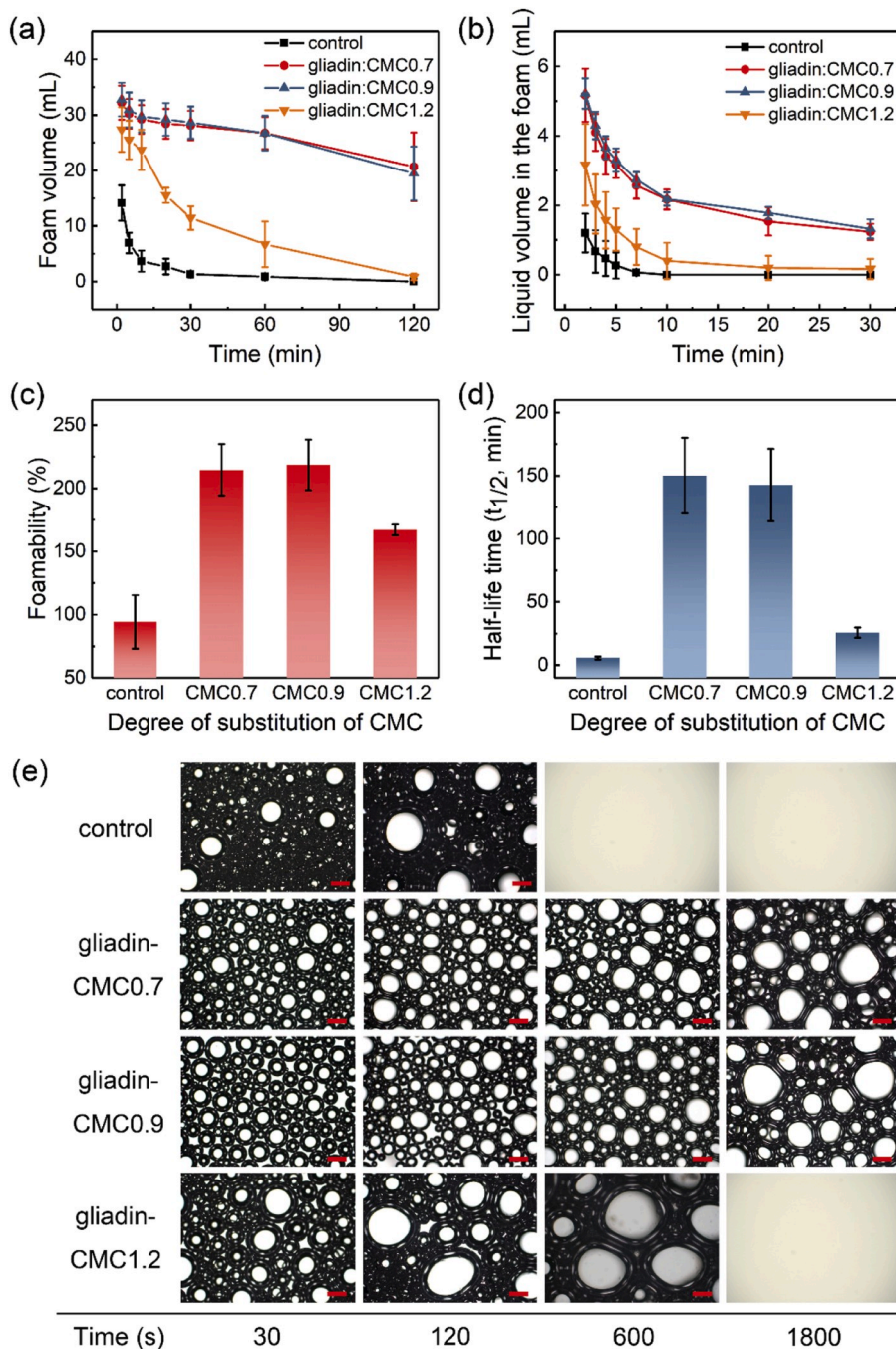


Fig. 6. (a) Foam decay curves, (b) liquid volume in foams, (c) foamability, and (d) half-life time ($t_{1/2}$, min) for foams generated by the control and G-CMC NPs with different DS of CMC. (e) Time evolution of air bubbles stabilized by the control and G-CMC NPs with different DS of CMC. Solid bars in all images correspond to a length of 1000 μm .

for interfaces stabilized by complex nanoparticles at all ratios was notably slower and less pronounced than that of the control. Moreover, G-CMC NPs at different ratios acquired comparable E_d values after oscillating for 3 h. For G-CMC NPs at all ratios, E_d exhibited a frequency-dependent behavior (Fig. 5d). With the increase of G:CMC ratio, the value of the scaling exponent n gradually rose (Fig. 5e). This reflected that the structures of the adsorption layers formed by G-CMC NPs exhibited solid-like behavior which was becoming somewhat less elastic

as the amount of CMC in the complex increased. Moreover, the E_d of the surface layers for all ratios also displayed an amplitude-dependent behavior (Fig. 5f). All ratios had a comparable shape of the Lissajous plots at the same amplitude (5–30%) (Fig. S1).

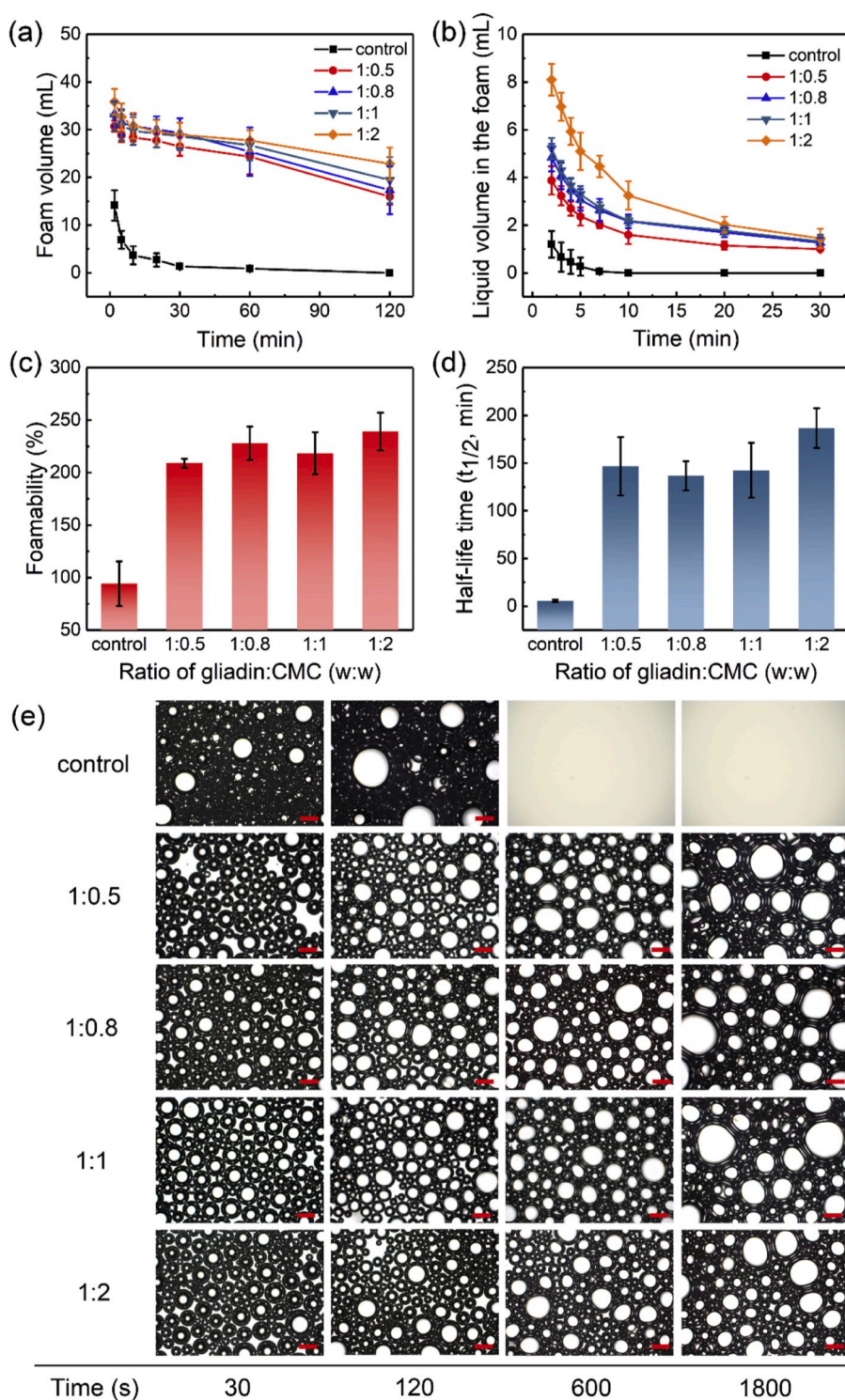


Fig. 7. (a) Foam decay curves, (b) liquid volume in foams, (c) foamability, and (d) half-life time ($t_{1/2}$, min) for foams generated by the control and G-CMC NPs with different G:CMC ratios. (e) Time evolution of air bubbles stabilized by the control and G-CMC NPs with different G:CMC ratios. Solid bars in all images correspond to a length of 1000 μm .

3.3. Foaming properties of gliadin-CMC nanoparticles

3.3.1. Effect of degree of substitution of CMC

Fig. 6 a-e presents the foaming properties of G-CMC NPs with a DS of 0.7–1.2. For all studied nanoparticles, the foam volume decreased progressively as a function of time (Fig. 6a and Fig. S2). The decrease rates of foam volume for G-CMC0.7 and G-CMC0.9 NPs were evidently slower than that of G-CMC1.2 NPs and the control, suggesting that G-CMC NPs with a DS of 0.7 and 0.9 possessed stronger abilities to protect the bubbles against coalescence and disproportionation. This illustrated that G-CMC NPs with DS of 0.7 and 0.9 had higher foam stability than those with a DS of 1.2 and the control. The initial foam volume and bubble size can be utilized to characterize the foamability (FA), where a higher amount of foam and smaller bubble size indicate a higher foamability (Peng et al., 2018; Wan, Yang, & Sagis, 2016b). As can be seen from Fig. 6c, e, and Fig. S2, G-CMC0.7 and G-CMC0.9 NPs could generate more foam with a smaller bubble size, and the FA was almost 2.5-fold larger than that of the control. This indicated that adding CMC with a DS of 0.7 and 0.9 to gliadin NP suspension could greatly improve its FA. It is worth mentioning that the G-CMC NPs with a DS of 0.7 and 0.9 displayed impressive FA (~220%), even though the concentration of gliadin (fixed at 1 mg/mL) was very low in the final solutions. The G-CMC1.2 NPs exhibited lower foamability and a bigger bubble size at 30 s, when compared with the other two DS. This might be the result from its slow adsorption rate to the air/water interface (Fig. 3b), resulting from the larger surface charge.

In general, foam stability (FS) can be quantified by liquid volume in the foam over time, half-life time ($t_{1/2}$), and changes of bubble size and shape with time. The corresponding experiments are performed and shown in Fig. 6b, d, and e. Compared with the control, the G-CMC NPs with DS of 0.7–1.2 had a higher liquid volume in the foam, a longer $t_{1/2}$, and a stronger resistance against bubble growth. This showed that the presence of CMC could increase the FS of gliadin NPs. In addition, the G-CMC0.7 and G-CMC0.9 NPs possessed a slower drainage rate, a longer $t_{1/2}$, and stronger capability to prevent bubble coalescence than G-CMC1.2. This indicated they acquired better FS. This might be due to the lower surface charge of these G-CMC NPs which resulted in a faster adsorption, and smaller and narrower initial bubble size distribution, which slowed down the liquid drainage, and the rate of coalescence and disproportionation.

3.3.2. Effect of gliadin-CMC ratio

The foam decay with time, the liquid volume in the foam over time, FA, and $t_{1/2}$ were monitored to estimate the foaming behaviors of G-CMC NPs at different G:CMC ratio (Fig. 7 a-d). A comparable FA and similar initial bubble size (30 s) were observed for G-CMC NPs at all ratios (Fig. 7c and e), indicating that all investigated ratios had high and similar foam capacity. The G-CMC NPs at a ratio of 1:2 possessed the slowest drainage rate, the longest $t_{1/2}$, and the strongest ability to prevent foam from coalescing of all four ratios (Fig. 7a, b, d, and Fig. S3). This implied G:CMC at 1:2 possessed a higher FS. All ratios had similar adsorption rate and comparable E_d of the surface layer, but the ratio of 1:2 had the highest viscosity among all ratios, which slowed down foam drainage, coarsening, and disproportionation more efficiently, and thus leading to the high FS.

Our results imply that the FA of the NPs is mainly determined by their adsorption rate. The G-CMC1.2 NPs had the slowest adsorption rate, due to their high negative surface charge, resulting in a strong electrostatic repulsion, thus leading to a slower adsorption behavior. Therefore, it had the lowest FA among three DS. The G-CMC NPs at different ratios possessed similar adsorption kinetics, and had comparable FA. All ratios showed similar E_d , but the ratio of 1:2 had the highest viscosity, which could slow down the drainage rate and protect the bubbles against coalescence, thus resulting in high FS.

4. Conclusions

The effects of DS of CMC and G:CMC ratio on the surface and foaming behaviors of G-CMC NPs were determined and three major implications were obtained. First, compared to gliadin NPs, G-CMC NPs at all DS and ratios possessed higher foamability and foam stability. Second, G-CMC0.7 and G-CMC0.9 NPs had a faster adsorption rate than G-CMC1.2 NPs, resulting from their lower negative surface charge. The adsorption rate was not affected by the G:CMC ratio. Third, the viscosity of the dispersions of G-CMC NPs also played an important role in stabilizing foams. These observations show that G-CMC NPs are a promising foaming agent, and have potential for application in the field of foamed food.

Declaration of competing interest

Authors declare that there are no known competing financial interests or personal relationships that could have appeared to influence the work reported in this paper.

The work described was original research that has not been published previously, and not under consideration for publication elsewhere, in whole or in part.

No conflict of interest exists in the submission of this manuscript, and the manuscript is approved by all authors for publication. All the authors listed have approved the manuscript that is enclosed.

CRediT authorship contribution statement

Dengfeng Peng: Investigation, Formal analysis, Validation, Data curation, Writing - original draft, Visualization. **Weiping Jin:** Investigation, Formal analysis, Validation, Data curation. **Miriam Arts:** Investigation, Formal analysis, Validation, Data curation. **Jack Yang:** Investigation, Formal analysis, Validation, Data curation. **Bin Li:** Conceptualization, Methodology, Writing - review & editing, Supervision. **Leonard M.C. Sagis:** Conceptualization, Methodology, Writing - review & editing, Supervision, Project administration.

Acknowledgments

Dengfeng Peng was financially supported by the International Postdoctoral Exchange Fellowship Program of the Office of China Postdoctoral Council (No. 20180081). This work was financially supported by the National Key R&D Program of China (Program No. 2017YFD0400205) & the National Natural Science Foundation of China (Grant No. 31772015).

Appendix A. Supplementary data

Supplementary data to this article can be found online at <https://doi.org/10.1016/j.foodhyd.2020.105955>.

References

- Asghari, A. K., Norton, I., Mills, T., Sadd, P., & Spyropoulos, F. (2016). Interfacial and foaming characterisation of mixed protein-starch particle systems for food-foam applications. *Food Hydrocolloids*, 53, 311–319.
- Babazadeh, A., Tabibiazar, M., Hamishehkar, H., & Shi, B. (2019). Zein-CMC-PEG multiple nanocolloidal systems as a novel approach for nutra-pharmaceutical applications. *Advanced Pharmaceutical Bulletin*, 9(2), 1–9.
- Banc, A., Desbat, B., Renard, D., Popineau, Y., Mangavel, C., & Navailles, L. (2007). Structure and orientation changes of ω - and γ -gliadins at the air–water interface: A PM–IRRRAS spectroscopy and Brewster angle microscopy study. *Langmuir*, 23(26), 13066–13075.
- Brush, L. N., & Roper, S. M. (2008). The thinning of lamellae in surfactant-free foams with non-Newtonian liquid phase. *Journal of Fluid Mechanics*, 616, 235–262.
- Chen, M., Bleeker, R., Sala, G., Meinders, M., van Valenberg, H., van Hooijdonk, A., et al. (2016). Particle size determines foam stability of casein micelle dispersions. *International Dairy Journal*, 56, 151–158.

- Cristofolini, L., Orsi, D., & Isa, L. (2018). Characterization of the dynamics of interfaces and of interface-dominated systems via spectroscopy and microscopy techniques. *Current Opinion in Colloid & Interface Science*, 37, 13–32.
- Dollet, B., & Raufaste, C. (2014). Rheology of aqueous foams. *Comptes Rendus Physique*, 15(8–9), 731–747.
- Ellis, A., Norton, A., Mills, T., & Norton, I. (2017). Stabilisation of foams by agar gel particles. *Food Hydrocolloids*, 73, 222–228.
- Gibis, M., Schuh, V., & Weiss, J. (2015). Effects of carboxymethyl cellulose (CMC) and microcrystalline cellulose (MCC) as fat replacers on the microstructure and sensory characteristics of fried beef patties. *Food Hydrocolloids*, 45, 236–246.
- Jambrak, A. R., Mason, T. J., Lelas, V., Paniwnyk, L., & Herceg, Z. (2014). Effect of ultrasound treatment on particle size and molecular weight of whey proteins. *Journal of Food Engineering*, 121, 15–23.
- Jia, W., Cui, B., Ye, T., Lin, L., Zheng, H., Yan, X., et al. (2014). Phase behavior of ovalbumin and carboxymethylcellulose composite system. *Carbohydrate Polymers*, 109, 64–70.
- Jin, H., Zhou, W., Cao, J., Stoyanov, S. D., Blijdenstein, T. B., de Groot, P. W., et al. (2012). Super stable foams stabilized by colloidal ethyl cellulose particles. *Soft Matter*, 8(7), 2194–2205.
- Jin, W., Zhu, J., Jiang, Y., Shao, P., Li, B., & Huang, Q. (2017). Gelatin-based nanocomplex-stabilized Pickering emulsions: Regulating droplet size and wettability through assembly with glucomannan. *Journal of Agricultural and Food Chemistry*, 65(7), 1401–1409.
- Liang, H., Huang, Q., Zhou, B., He, L., Lin, L., An, Y., et al. (2015). Self-assembled zein-sodium carboxymethyl cellulose nanoparticles as an effective drug carrier and transporter. *Journal of Materials Chemistry B*, 3(16), 3242–3253.
- Liu, F., & Tang, C. H. (2014). Emulsifying properties of soy protein nanoparticles: Influence of the protein concentration and/or emulsification process. *Journal of Agricultural and Food Chemistry*, 62(12), 2644–2654.
- Li, Z., Wang, Y., Pei, Y., Xiong, W., Xu, W., Li, B., et al. (2017). Effect of substitution degree on carboxymethylcellulose interaction with lysozyme. *Food Hydrocolloids*, 62, 222–229.
- Lucassen, J., & Van Den Tempel, M. (1972). Dynamic measurements of dilatational properties of a liquid interface. *Chemical Engineering Science*, 27(6), 1283–1291.
- Mahmoudi, N., Axelos, M. A., & Riaublanc, A. (2011). Interfacial properties of fractal and spherical whey protein aggregates. *Soft Matter*, 7(17), 7643–7654.
- Matsumiya, K., & Murray, B. S. (2016). Soybean protein isolate gel particles as foaming and emulsifying agents. *Food Hydrocolloids*, 60, 206–215.
- Morales, R., Martínez, K. D., Ruiz-Henestrosa, V. M. P., & Pilosof, A. M. (2015). Modification of foaming properties of soy protein isolate by high ultrasound intensity: Particle size effect. *Ultrasonics Sonochemistry*, 26, 48–55.
- Murray, B. S., & Ettelaie, R. (2004). Foam stability: Proteins and nanoparticles. *Current Opinion in Colloid & Interface Science*, 9(5), 314–320.
- Patino, J. M. R., Sanchez, C. C., & Niño, M. R. (2008). Implications of interfacial characteristics of food foaming agents in foam formulations. *Advances in Colloid and Interface Science*, 140(2), 95–113.
- Peng, D., Jin, W., Li, J., Xiong, W., Pei, Y., Wang, Y., et al. (2017). Adsorption and distribution of edible gliadin nanoparticles at the air/water interface. *Journal of Agricultural and Food Chemistry*, 65(11), 2454–2460.
- Peng, D., Jin, W., Tang, C., Lu, Y., Wang, W., Li, J., et al. (2018). Foaming and surface properties of gliadin nanoparticles: Influence of pH and heating temperature. *Food Hydrocolloids*, 77, 107–116.
- Peng, D., Yang, J., Li, J., Tang, C., & Li, B. (2017). Foams stabilized by beta-lactoglobulin amyloid fibrils: Effect of pH. *Journal of Agricultural and Food Chemistry*, 65(48), 10658–10665.
- Rühs, P. A., Affolter, C., Windhab, E. J., & Fischer, P. (2013). Shear and dilatational linear and nonlinear subphase controlled interfacial rheology of β -lactoglobulin fibrils and their derivatives. *Journal of Rheology*, 57(3), 1003–1022.
- Rühs, P. A., Scheuble, N., Windhab, E. J., & Fischer, P. (2013). Protein adsorption and interfacial rheology interfering in dilatational experiment. *The European Physical Journal - Special Topics*, 222(1), 47–60.
- Sagis, L. M. C., & Fischer, P. (2014). Nonlinear rheology of complex fluid–fluid interfaces. *Current Opinion in Colloid & Interface Science*, 19(6), 520–529.
- Sagis, L. M. C., & Scholten, E. (2014). Complex interfaces in food: Structure and mechanical properties. *Trends in Food Science & Technology*, 37(1), 59–71.
- Salonen, A., In, M., Emile, J., & Saint-Jalmes, A. (2010). Solutions of surfactant oligomers: A model system for tuning foam stability by the surfactant structure. *Soft Matter*, 6(10), 2271–2281.
- Schmitt, C., Bovay, C., & Rouvet, M. (2014). Bulk self-aggregation drives foam stabilization properties of whey protein microgels. *Food Hydrocolloids*, 42, 139–148.
- Schmitt, C., Bovay, C., Rouvet, M., Shojaei-Rami, S., & Kolodziejczyk, E. (2007). Whey protein soluble aggregates from heating with NaCl: Physicochemical, interfacial, and foaming properties. *Langmuir*, 23(8), 4155–4166.
- van den Berg, M. E. H., Kuster, S., Windhab, E. J., Sagis, L. M. C., & Fischer, P. (2018). Nonlinear shear and dilatational rheology of viscoelastic interfacial layers of cellulose nanocrystals. *Physics of Fluids*, 30(7), 072103.
- van Kempen, S. E., Schols, H. A., van der Linden, E., & Sagis, L. M. (2013). Non-linear surface dilatational rheology as a tool for understanding microstructures of air/water interfaces stabilized by oligofructose fatty acid esters. *Soft Matter*, 9(40), 9579–9592.
- Wan, Z., Yang, X., & Sagis, L. M. (2016a). Contribution of long fibrils and peptides to surface and foaming behavior of soy protein fibril system. *Langmuir*, 32(32), 8092–8101.
- Wan, Z., Yang, X., & Sagis, L. M. (2016b). Nonlinear surface dilatational rheology and foaming behavior of protein and protein fibrillar aggregates in the presence of natural surfactant. *Langmuir*, 32(15), 3679–3690.
- Wang, J. M., Xia, N., Yang, X. Q., Yin, S. W., Qi, J. R., He, X. T., et al. (2012). Adsorption and dilatational rheology of heat-treated soy protein at the oil-water interface: Relationship to structural properties. *Journal of Agricultural and Food Chemistry*, 60(12), 3302–3310.
- Wege, H. A., Kim, S., Paunov, V. N., Zhong, Q., & Velez, O. D. (2008). Long-term stabilization of foams and emulsions with in-situ formed microparticles from hydrophobic cellulose. *Langmuir*, 24(17), 9245–9253.
- Wu, Y., Fang, S., Zhang, K., Zhao, M., Jiao, B., & Dai, C. (2018). Stability mechanism of nitrogen foam in porous media with silica nanoparticles modified by cationic surfactants. *Langmuir*, 34(27), 8015–8023.
- Wu, N. N., Zhang, J. B., Tan, B., He, X. T., Yang, J., Guo, J., et al. (2014). Characterization and interfacial behavior of nanoparticles prepared from amphiphilic hydrolysates of beta-conglycinin-dextran conjugates. *Journal of Agricultural and Food Chemistry*, 62(52), 12678–12685.
- Xiong, W., Deng, Q., Li, J., Li, B., & Zhong, Q. (2020). Ovalbumin-carboxymethylcellulose complex coacervates stabilized high internal phase emulsions: Comparison of the effects of pH and polysaccharide charge density. *Food Hydrocolloids*, 98, 105282.
- Zhou, F.-Z., Yu, X.-H., Zeng, T., Yin, S.-W., Tang, C.-H., & Yang, X.-Q. (2019). Fabrication and characterization of novel water-insoluble protein porous materials derived from Pickering high internal-phase emulsions stabilized by gliadin-chitosan-complex particles. *Journal of Agricultural and Food Chemistry*, 67(12), 3423–3431.